Rapid Design of Fully Soft Deployable Structures Via Kirigami Cuts and Active Learning

Leixin Ma, Mrunmayi Mungekar, Vwani Roychowdhury,* and M.K. Jawed**

Soft deployable structures – unlike conventional piecewise rigid deployables based on hinges and springs – can assume intricate 3-D shapes, thereby enabling transformative soft robotic and manufacturing technologies. Their virtually infinite degrees of freedom allow precise control over the final shape. The same enabling high dimensionality, however, poses a challenge for solving the inverse problem: fabrication of desired 3D structures requires manufacturing technologies with extensive local actuation and control, and a trial-and-error search over a large design space. Both of these shortcomings are addressed by first developing a simplified planar fabrication approach that combines two ingredients: strain mismatch between two layers of a composite shell and kirigami cuts that relieves localized stress. In principle, it is possible to generate targeted 3-D shapes by designing the appropriate kirigami cuts and the amount of prestretch (without any local control). Second, a data-driven physics-guided framework is formulated that reduces the dimensionality of the inverse design problem using autoencoders and efficiently searches through the "latent" parameter space in an active learning approach. The rapid design procedure is demonstrated via a range of target shapes, such as peanuts, pringles, flowers, and pyramids. Experiments and our numerical predictions are found to be in good agreement.

1. Introduction

Morphing planar geometry to 3D shapes can find a wide variety of engineering applications[1] from additive and subtractive manufacturing to soft actuators[2,3] and architecture.[4–6] Multiple mechanisms have been reported for the 2D to 3D transformation, including residual stress-induced bending,[7] temperature-induced growth,[8] inflatable membranes,[9] composite materials controlled by external stimuli (e.g., temperature and pH),[1] paper folding,[10] swelling,[11] mechanical loads, and boundary conditions.[12–14] The fabrication of these shape-morphing structures often requires detailed local control of the geometry, curvature, and stress.[1,7,9,13–19] Even though optimizing and realizing arbitrary 3D deformed shapes, such as a human face, is possible, this is often done at a cost of complicated fabrication technique.[1,20] Moreover, the inverse design problem of optimizing the physical parameters to achieve the targeted shape typically requires a trial and error search over a high-dimensional space.

Is it possible to rapidly design targeted shape-morphing structures by using structural global instability? To address such problems, this work introduces a new paradigm for planar manufacturing. A soft kirigami composite (a bilayer shell) deforms from 2D plane to the target 3D shape due to two key mechanisms, which are the kirigami (i.e., material removal)[3,21–23] and strain mismatch.[24,25] Due to the strain mismatch between the layers, the structure experiences global out-of-plane buckling. Compared to fabrication techniques requiring precise control of various parts of the structure, the reported technique first developed in ref. [26] is much easier to implement.

Nevertheless, the convenience of this manufacturing approach alone may not ensure its widespread adoption. To achieve programmability of diverse classes of target shapes, we need to locally learn how to remove materials, by introducing specific kirigami cut patterns. Otherwise, the buckling patterns may be limited to only a few buckling modes.[24,26]

Then, the design problem reduces to rapidly optimizing kirigami patterns in 2D (i.e., marking the areas where material has to be removed) that would morph the planar structure to a desired 3D shape. However, kirigami cuts have highly nonlocal impact on the structure. A cut at a certain location may affect the

---

L. Ma, M. Mungekar, M. Jawed
Dept. of Mechanical and Aerospace Engineering
University of California
Los Angeles, CA 90095, USA
E-mail: leixin.ma@asu.edu; khalidjm@seas.ucla.edu

L. Ma
School for Engineering of Matter, Transport & Energy
Arizona State University
Tempe, AZ 85287, USA

V. Roychowdhury
Dept. of Electrical and Computer Engineering
University of California
Los Angeles, CA 90095, USA
E-mail: vwani@g.ucla.edu

The ORCID identification number(s) for the author(s) of this article can be found under https://doi.org/10.1002/admt.202301305

DOI: 10.1002/admt.202301305

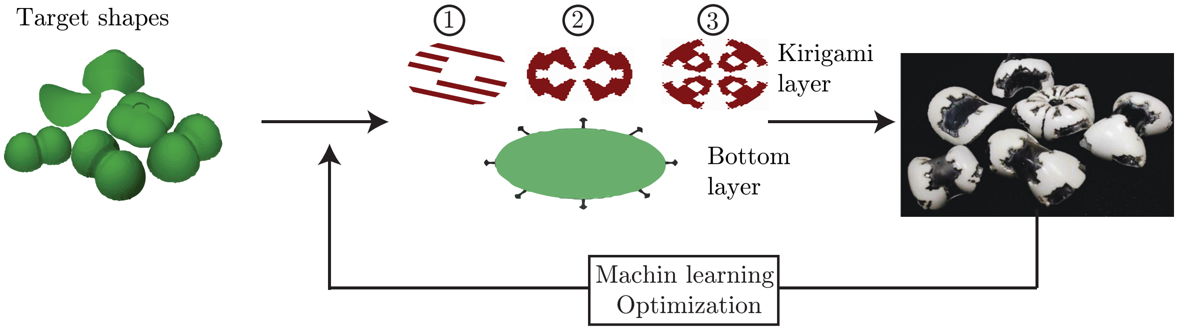

Figure 1. The inverse problem aims at designing target 3D shapes by finding the optimal fabrication strategies. Six target shapes are shown on the left, while the six experimental results of soft kirigami composites correspond to the target shapes shown on the right. The planar fabrication uses a kirigami layer and a bottom layer under radial prestrech is shown in the middle. For the kirigami layers, we considered three classes kirigami patterns, 1) unidirectional strips, 2) reflectional symmetry, and 3) fourfold radial symmetry. The machine learning-based optimization is conducted iteratively until the manufactured soft kirigami composite sufficiently resembles the target shapes.

global shape of the deformed shell. Hence, the kirigami pattern optimization for target 3D shapes cannot be conducted locally in space, but requires a global approach to explore the large design space.

Such inverse design problems where new structures and materials are designed for target functionalities have received a significant boost from recent advances in machine learning (ML). Various ML algorithms, such as Variational Autoencoder (VAE)[27,28] and Generative Adversarial Network[29,30] have been successfully applied. However, most of these ML-aided inverse design methods still depend on the generation of a computationally prohibitive number of forward simulation data.[29,31] A network is then trained to learn the inverse map in a supervised manner, with the output of the forward simulation used as input, and the corresponding design parameters as the desired output. This computational overhead of generating forward simulation data is particularly severe for our case. Given a kirigami pattern and other parameters, it takes minutes of computing time to generate corresponding 3D shapes. To train an inverse ML system, one could require millions of such forward simulations, making such inverse approaches computationally intractable for our application.

In this paper, to solve the global design and optimization problem for buckling-induced morphing soft composites, we make a judicious use of recent advances in dimension reduction techniques (e.g., VAEs), and integrate them with active learning techniques (e.g., Bayesian optimization), where forward computations are done on-demand. Such active learning techniques, when used by themselves, typically do not work well for high-dimensional search spaces in our application. The use of model reduction techniques of ML makes these methods practicable. We commence by generating sets of candidate kirigami patterns with symmetry properties mirroring the target 3D shape. A VAE parameterizes these symmetric patterns using low-dimensional latent features, thereby reducing the dimensionality of the inverse problem and enabling the generation of more versatile patterns compared to alternatives.[32] Subsequently, we iteratively seek optimal latent features using the Bayesian Optimization framework.[33] We validate our approach through numerical simulations and controlled tabletop experiments, successfully generating target 3D shapes with various symmetric properties. The strong agreement between experimental results and simulations highlights the potential of this method for algorithmic metamaterial design.

2. Overall Concept

2.1. Problem Description

The inverse problem aims at designing target 3D shapes by finding the optimal fabrication strategies, as shown in **Figure 1**. The proposed fabrication technique is shown in **Figure 2***A*(i) to *A*(ii). We start from two thin, flexible and stretchable plates (Figure 2*A*(i)). The maximum radius of the top layer is *R*. First, strain mismatch between two plates or layers is created by radially stretching the bottom one with the amount of prestretch λ (Figure 2*A*(ii)). Then, the top layer of the same radius as the stretched bottom layer is glued onto the bottom layer (Figure 2*A*(iii)). The strain mismatch between the two layers induces out-of-plane buckling (Figure 2*A*(iv)), since bending is less energetically expensive than compression for thin shells.[11] However, using strain mismatch in composite shells yields a limited number of structural modes,[24,26] and the elastic shells may easily wrinkle (localized deformation) to relax the compressive stresses instead of a global change in shape.[34] Hence, material needs to be strategically removed from the top layer to create kirigami patterns in order to yield a target 3D shape. The theoretical characterization of these kirigami-aided stress relief is still not fully available. The material removal expands the possible number of attainable 3D shapes from 2D, with the out-of-plane buckling depending on both the magnitude of prestretch and geometric parameters (including kirigami cuts).[35,36] Based on this rapid fabrication technique, we aim at inversely designing the optimal kirigami patterns, size of the structure (measured by radius *R*), and prestretch λ such that a target 3D shape can be achieved.

2.2. Machine Learning Framework for Design of Soft Kirigami Composite Structure

To tackle the challenges of Edisonian searches, our machine learning-aided design process is illustrated in Figure 2*B*(i),(ii), and discussed in more detail below.

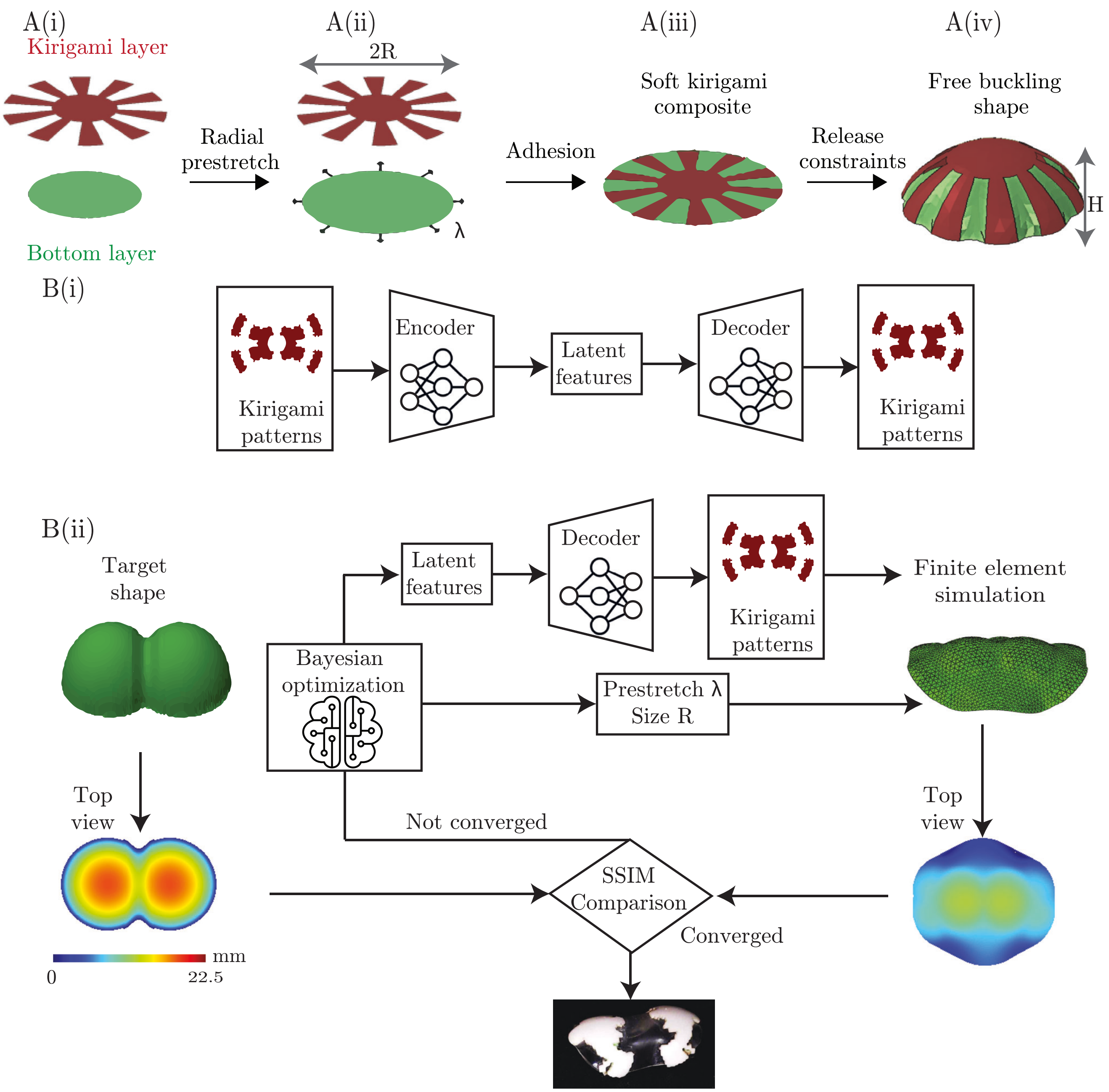

Figure 2. A) Overview of the fabrication concept: The composite structure with a kirigami layer and a substrate layer bend to a free buckling shape under radial prestretch. B) Flow chart of the data-driven design and optimization of soft kirigami composite. B(i) A VAE to reduce the dimension of kirigami patterns to a small number of latent variables. B(ii) A Bayesian Optimization loop that iteratively searches the optimal combination of latent kirigami pattern variables, size of the structure, and amount of prestretch that results to the target 3D topology.

2.3. Dimension Reduction: Compact and Continuous Representation of Kirigami Patterns

A kirigami pattern can be represented by an $N \times N$ binary image, where the pixels in the uncut areas are represented by 1's. This would correspond to a very high (N^2) dimensional search space. Recent advances in Computer Vision (CV), however, have shown that such a family of images typically lies on a much smaller dimensional (say D) manifold, referred to as the latent space. One can then search only over a D-dimensional space (e.g., $D = 6$ in our design), leading to considerable computational savings. A VAE is one ideal computational model that can be used to learn a generative model of kirigami patterns by learning the underlying distribution of the patterns to generate new samples from that distribution. In a VAE model, a) every kirigami image can be mapped to a D-dimensional vector using an Encoder network, and b) every D-dimensional vector in the latent space can be mapped to a sample kirigami image using a Decoder network.

The Encoder and Decoder networks are trained simultaneously, such that the latent features are representative enough for various kirigami patterns. Once trained, any active learning framework can view the space of kirigami patterns as a *D*-dimensional continuous space. This allows one to train the VAE using only a limited set of representative kirigami patterns, and using the VAE to interpolate and generate potentially infinite number of similar kirigami patterns. The detailed architecture and hyperparameters for the VAE are described in the Supporting Information Text.

2.4. Design of Numerical Experiments Using Active Learning

Optimal design parameters, including the kirigami latent features (*D*-dimensional), structure size (measured by radius), and prestretch that yield the target 3D shape, were searched by performing iterative Bayesian Optimizations, as shown in Figure 2*B*(ii), which is one kind of active learning method. The detailed algorithm for active learning is described in *Experimental Section*. To search global optimums, the optimization aims to "explore" (prioritizing regions with large uncertainty) and "exploit" (focusing on the regions with minimum loss function) the high dimensional parametric spaces, until a suitable loss function is minimized.[37]

To initialize the optimization process, we randomly sampled ten combinations of latent features, structure sizes, and prestretches. For each combination of the proposed kirigami patterns and prestretch, numerical experiments were performed via finite element simulations. A Gaussian process regression model was constructed to approximate the unknown effect of the design variables on the loss function, which is the error of the 3D shape between the simulations and the design target. A common way to represent 3D data is via the projected image of the height.[38] The negative structural similarity index is chosen as the loss function, which is used to characterize the dissimilarity between two images. Compared to the mean squared error, the structural similarity index (SSIM) is a perceptually-motivated loss function, which is found to have better performance for image restoration tasks than the squared l_2 norm of the error.[39] The SSIM ranges between 0 and 1, where values closer to 1 indicate a higher degree of similarity between two images. A detailed definition of the SSIM is included in the Supporting Information Text.

Once the Gaussian process model is constructed, an expected improvement function,[33] that increases with both the mean of the loss function and its uncertainty, is calculated, as described in *Experimental Section*. Then, the combination of latent features trained per kirigami pattern family, size of the structure, and prestretch that maximizes the expected improvement function is selected. The corresponding kirigami patterns for that combination of latent features can be recovered from the trained decoder network. The recovered patterns are used to create the mesh for the kirigami layer to perform the next round of finite element simulation. The negative SSIM between the results of finite element simulation and target shape is used to update the Gaussian process model and reassess the expected improvement function. Such a process continues iteratively. Once the optimization converges, we verify its effectiveness using precision desktop experiments.

2.5. Generation of Candidate Kirigami Patterns for VAE Training

We tested the performance of three classes of candidate kirigami patterns, as shown in **Figure** 3*A*(i) to (iii). The first class, as shown in Figure 3*A*(i), is made of uni-directional fibers. For example, Hanakata et al.[27] demonstrated that the uni-directional patterns have good expressive power and can be used to interpolate a variety of mixed kirigami cuts. The other classes of kirigami patterns exhibit the same type of symmetric property as the target 3D shapes, as shown in Figure 3*A*(ii),(iii). We will see later in the paper that the peanut and pringle-like shapes have reflectional symmetry with respect to the two principal axes, while the flower shape has fourfold radial symmetry. To create symmetric kirigami patterns, the kirigami cuts are created in certain regions, with the patterns in the remaining regions directly created via rotations or reflections (see *Supporting Information Text*). Both types of non-symmetric and symmetric patterns are augmented via rotation. After rotating the kirigami patterns two to four times, the total number of images for each class is 40955, 40955, and 24573, respectively. These images are used to train VAE models to find low-dimensional representations.

3. Physical and Numerical Experiments

3.1. Desktop-Scale Physical Experiments

Figure 3*B*(i) to (iv) present our experimental setup and the key steps in fabrication. The experimental setup consists of four linear translation stages (250 mm travel, Thorlabs). The substrate and the kirigami layers are made of hyper-elastic materials (3M, VHB tapes). We used a laser cutter to cut the desired kirigami patterns. In the process, if there are a lot of isolated pieces of the kirigami design, during the fabrication, we maintain a minimal connection between the isolated pieces (such as a bounding circle which can be easily cut-off later) until the moment they are positioned on the substrate. If the isolated pieces are too small (order of magnitude of approximately 2mm), they can be ignored with no effect on the final shape. A large substrate layer is applied with the four corners fixed to the four stages (Figure 3*B*(i)). Then, to impose the radial strain upon the substrate, we stretch the substrate layer with the same amount in the horizontal and vertical directions (Figure 3*B*(ii)). Once stretching is complete, a kirigami layer is glued on top of the substrate (Figure 3*B*(iii)). We ensure that the central region of the substrate layer – onto which the kirigami layer is glued – is uniformly stretched, not affected by the boundaries. Afterward, Figure 3*B*(iv) shows that the excess substrate is cut away along the outline of the circular substrate. The composite structure then morphs to a certain 3D shape due to the strain mismatch in the two layers.

3.2. Finite Element-Based Numerical Simulations

The finite element software, Abaqus,[40] is used to model the nonlinear large deformation of the hyper-elastic composite structures. In the simulations, we use incompressible Mooney Rivlin model to simulate the hyper-elastic materials of the substrate and the kirigami layer being tested. The material constants in

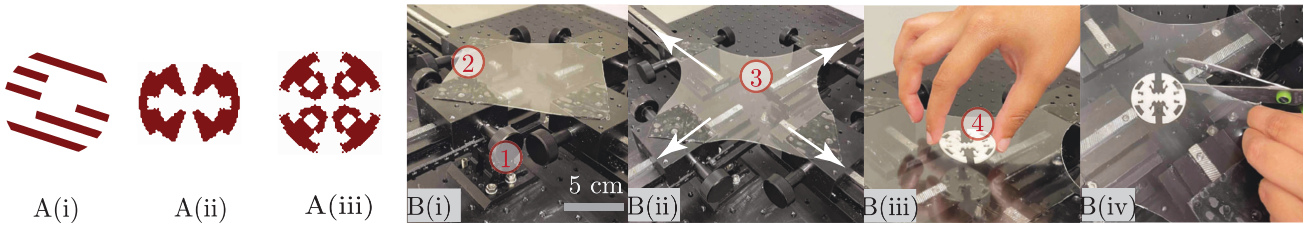

Figure 3. A) Examples of different classes of kirigami patterns: A(i) unidirectional fibers, A(ii) shapes of reflectional symmetry with two lines of symmetry, A(iii) fourfold radial symmetry. B) Experimental setup. B(i) Schematic representation of the system consist of two-knob stages (1) on 250 mm tracks (2) knobs to adjust the stage location. B(ii) Snapshot of the system when the substrate layer (3) is stretched. B(iii) Attach a kirigami layer (4) on top of the substrate layer. B(iv) Release the prestretch by cutting along the outline of the circular substrate.

the model C_1 and C_2 for the substrate and the kirigami layers are listed in **Table 1**. Each layer of the composite structure is modeled as a shell to reduce the computational cost. In the finite element simulations, the substrate and kirigami layers are meshed using three-node triangular shell elements. The substrate layer was divided into 2772 triangle elements. The number of elements are found to be large enough to prevent wrinkling, and stress concentration. The material properties for the substrate and kirigami layer are listed in Table 1. The two shell structures are constrained so that their normals match. The center of the composite structure is fixed. The prestretch is modeled as isotropic thermal expansion (see *Supporting Information Text*). The equivalent temperature corresponding to the prestretch is computed. Then, the dynamics of the composite structure (for the given candidate kirigami pattern) is modeled by ABAQUS as the substrate is cooled back to the reference temperature. The resulting 3D shape is obtained after each such simulation converges. A nonlinear quasi-static simulation is conducted for each design inputs.

The final 3D shape when the active learning search converges will be referred to as the optimal predicted shape; the corresponding kirigami patterns, radius, and prestretch are the predicted optimal parameters. The detailed structural properties of the composite structure are included in the "Experimental Section". The numerical simulation is the most time-consuming step, which takes about 1–3 min wall clock time on a desktop computer (Ryzen 2950wx CPU @ 2.4 GHz). In total, 100 simulations take about 5 h. Since forward simulations are expensive, cutting down the number of runs is important. In this study, we are able to reduce the total number of forward runs from millions to just around 100, while obtaining accurate target shapes. Such computational tractability without compromising performance is one of the key advantages of the proposed machine learning-aided framework.

Table 1. Material parameters for the substrate and kirigami layer.

Parameter	Value
C_1^s	2.4 KPa
C_2^s	23.4 KPa
Thickness t^s	1.1 mm
C_1^k	-2.6 KPa
C_2^k	185.8 KPa
Thickness t^k	1.4 mm
Outer radius of the circular substrate	30 mm

4. Results

In this section, we test drive the framework with a few example target shapes with different distributions of curvatures and symmetric properties. We have described the details to mathematically generate target shapes in the *Supporting Information Text*. During the optimization, the range of radii of the kirigami structure is constrained between 24 mm and 39 mm while the amount of prestretch $\lambda = 1 + \epsilon$ is searched between 1.05 to 1.4, which means that the bottom layer is stretched by $\epsilon = 5\%$ to $\epsilon = 40\%$ along both directions.

4.1. Target 3D Shapes with Two Axes of Reflectional Symmetry

As an exemplar of this class, we pick a bilobe structure, resembling a peanut, as the target shape. Automatically generated 40,955 (64 by 64) binary kirigami images with reflectional symmetry are used to train the VAE. After experimenting on different sizes of latent features in Supporting Information text, we find that just a 6D latent space can reconstruct the training kirigami data with very high accuracy (measured by SSIM ≈ 0.97). Thus, the search space of kirigami patterns have been reduced from a 4096D binary image space to only a 6D continuous search space. New kirigami patterns can be generated by the VAE, and they are also found to exhibit reflectional symmetry, as demonstrated in the *Supporting Information Text*. More importantly, as demonstrated in **Figure 4**, the interpolated new kirigami patterns are often needed to generate 3D shapes that best match the target shapes. We next illustrate some of the salient characteristics of our inverse design framework.

4.2. Search Trajectory in the SSIM Space

The evolution of the design solutions via iterations to create a target peanut shape is demonstrated in Figure 4A and Movie S1 (Supporting Information). The red dots in Figure 4A plots the variation of SSIM over iterations. The maximum SSIMs before certain iteration steps are connected via the blue line. The maximum SSIM improves significantly from 0.7 (in the first ten random searches) to around 0.91 over time. Some red dots are

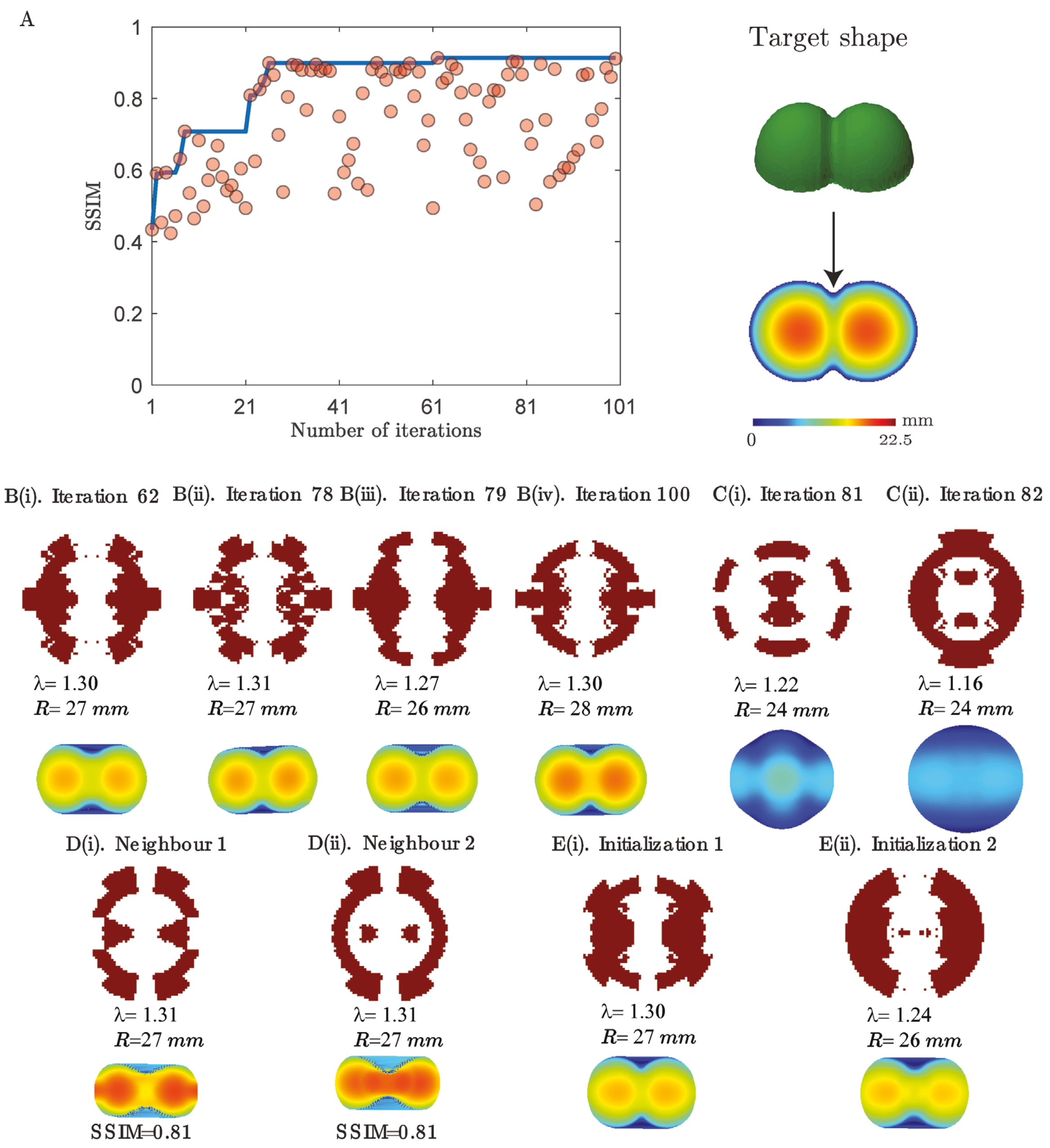

Figure 4. A) Search trajectory Variation of SSIM between target peanut shape and predicted free buckling shape over iterations. B) Multiple optimal solutions B1–B4)The top four optimal design solutions, including the kirigami patterns, prestretch and kirigami size. The corresponding height distribution for each design is presented at the bottom. C) Exploration during optimization C(i)–C(ii))Two examples showing the algorithm explores new kirigami patterns, that does not lead to closer solutions. D) Interpolated kirigami patterns are often required to better approximate target 3D shapes: D(i)–D(ii)) Two nearest neighbors for kirigami patterns found at iteration No. 78, whose free buckling shape gives lower SSIM. E) Effect of initialization E(i)-E(ii)) We tested different initialization of the Bayesian Optimization, and presented the results of optimized design parameters and free buckling shape over 100 iterations.

clustered near the optimal blue line, while some others scatter around the blue line. This suggests that during the Bayesian optimization, the model explores and exploits the design space interchangeably. It will not only locally exploit optimal solutions (such as between iteration 78 and 79 in Figure 4*B*, with materials concentrated to the left and right sides), but also explore unknown design space (such as iteration 81 and 82 in Figure 4*C*. More materials cover the top and bottom side of the planar structure).

4.3. Multiple Optimal Solutions Give SSIM Around 0.9 out of 1

Figure 4*B* shows that multiple latent feature combinations can lead to similar 3D deformed shapes. The prestretch and radius are important in governing the total elastic energy of the composite structure. The similar prestretches and radius for optimal peanut shapes suggests similar elastic energy is required to buckle 2D shapes to the peanut-like 3D shapes. Even though these optimal patterns look different, they share the common characteristics of having more material concentrated near the left and right ends of the kirigami. The different kirigami patterns suggest that not every material in the kirigami layer is important in affecting the global buckling-induced 3D shapes. While, the similarity suggests that the regions with more material compress the bare regions in between where the stiffness is lower, and such a compression leads to a ridge in the middle.

4.4. Interpolated Kirigami Patterns are Often Required to Better Approximate Target 3D Shapes

We also explored the generalization capability of VAE and the role it plays in optimization. For example, the optimal design shown in Figure 4*B2* is an interpolated pattern generated by the VAE, and not in the patterns used to train it. We find the nearest neighbors of this optimal generated pattern using K-nearest neighbors algorithm.[41] If we replace the generated pattern with its neighbors in Figure 4*D*, we find a decrease in the SSIM. This suggests the importance of interpolation capability in the latent space to achieve more accurate design solutions.

4.5. The Optimal Solutions can be Different to the Initializations

We repeat the optimization process several times with different initializations (described in *Supporting Information Text*). For different initializations that lead to similar values of SSIM (around 0.91) over 100 iterations, the optimized kirigami patterns are different from each other, as presented in Figure 4*E(i),(ii)*. However, the optimized prestretch and the radius are close to each other. This suggests that there exists a region of optimal strain-mismatch and structural size that leads to the target 3D shape.

Besides the peanut shapes in **Figure** 5*A*, we also use the same class of input kirigami patterns to create a pringle and a ship hull-like 3D shape, presented in Figure 5*B, C*. The optimized SSIM over 100 iterations is as high as 0.92 and 0.90, respectively. While the maximum SSIM over ten random searches is at 0.70 and 0.73, respectively. This suggests the importance of strategic search in creating target shapes. The largest errors are found to be near the sharp edges, where the local curvature has sharp changes.

4.6. Target 3D Shapes with FourFold Radial Symmetry

Inspired by flowers in nature and man-made pyramids, we further aim to create two corresponding deformed soft structures. Both targets are composed of shapes of fourfold radial symmetry. For example, for each petal in a flower, the structure is bilaterally symmetric, where each half is a mirror image of the other half. The generation of such radially symmetric kirigami patterns are described in *Supporting Information Text*. These kirigami patterns can also be represented by six latent features, without sacrificing the high reconstruction accuracy (measured by SSIM ≈ 0.99). As shown in Figure 5, we get very high SSIM. For the flower-like shape, the maximum SSIM increases from 0.81 in the first ten random combinations to 0.92 within 100 iterations. The maximum SSIM slightly increases from 0.83 in the first ten random searches to 0.87 for the pyramid shape.

4.7. Experimental Validation

We carried out the entire end-to-end design process involving five shapes, shown in Figure 5. We picked one optimal design for each target shape from our algorithm. Next, we used these optimal design parameters to manufacture the corresponding 3D structures. As Figure 5 shows, the target, the predicted and the manufactured 3D shapes have the same structural forms, validating our design process. Given such structural similarity, the maximum height (H) of the 3D structure is an easily measured metric for comparison. As shown in the fifth and the sixth columns of Figure 5, the H values are in good agreement between the predicted and manufactured 3D structures.

Meanwhile, we also find good agreement measured by other shape metrics. For example, for the optimal peanut-shaped structure we predicted in the simulation, the maximum length and width are 44 and 29 mm, respectively. While the maximum length and width of the fabricated peanut are 42 and 28 mm, respectively. The maximum width of the flower shape is 50 mm, which is also close to 49.8 mm measured in the experiment. In section 5.5, we employ a 3D scanning technology to conduct a more detailed local comparison in the shapes between predictions and experiments.

One can further explore the physics of the kirigami patterns discovered by our design framework. For example, for the fourfold radial symmetry involving the flower and the pyramid target shapes, the optimal kirigami patterns are shown in Figure 5*D, E*. The kirigami pattern for the flower shape has materials concentrated in the four lobes and has material removed in the center. This can explain the final shape: the bending of the areas covered with kirigami creates a ridge of slightly lower height in the middle, giving rise to the four lobed flower pattern. In contrast, the pyramid shape with the maximum height in the center requires more material concentrated in the center, as shown in Figure 5*D*.

5. Discussion

5.1. Kirigami Invariance: Scaling Law

We address the problem of manufacturing the same shape but with different scales (e.g., pyramids with different heights), without having to solve for optimal design parameters for each scale. Recall that designing a target 3D shape requires around hundreds of optimization steps, each involving an expensive forward simulation step. Thus, if we can identify a scaling law involving the radius R, prestretch λ, and the scale of the target shapes –while fixing the kirigami patterns– then such a scaling law can guide designers to quickly vary the scale of the deployable 3D soft structures.

For a given material property and kirigami pattern, the maximum normalized height H/R is affected by prestretch $\lambda = 1 + \epsilon$, and normalized radius R/t, where H is the

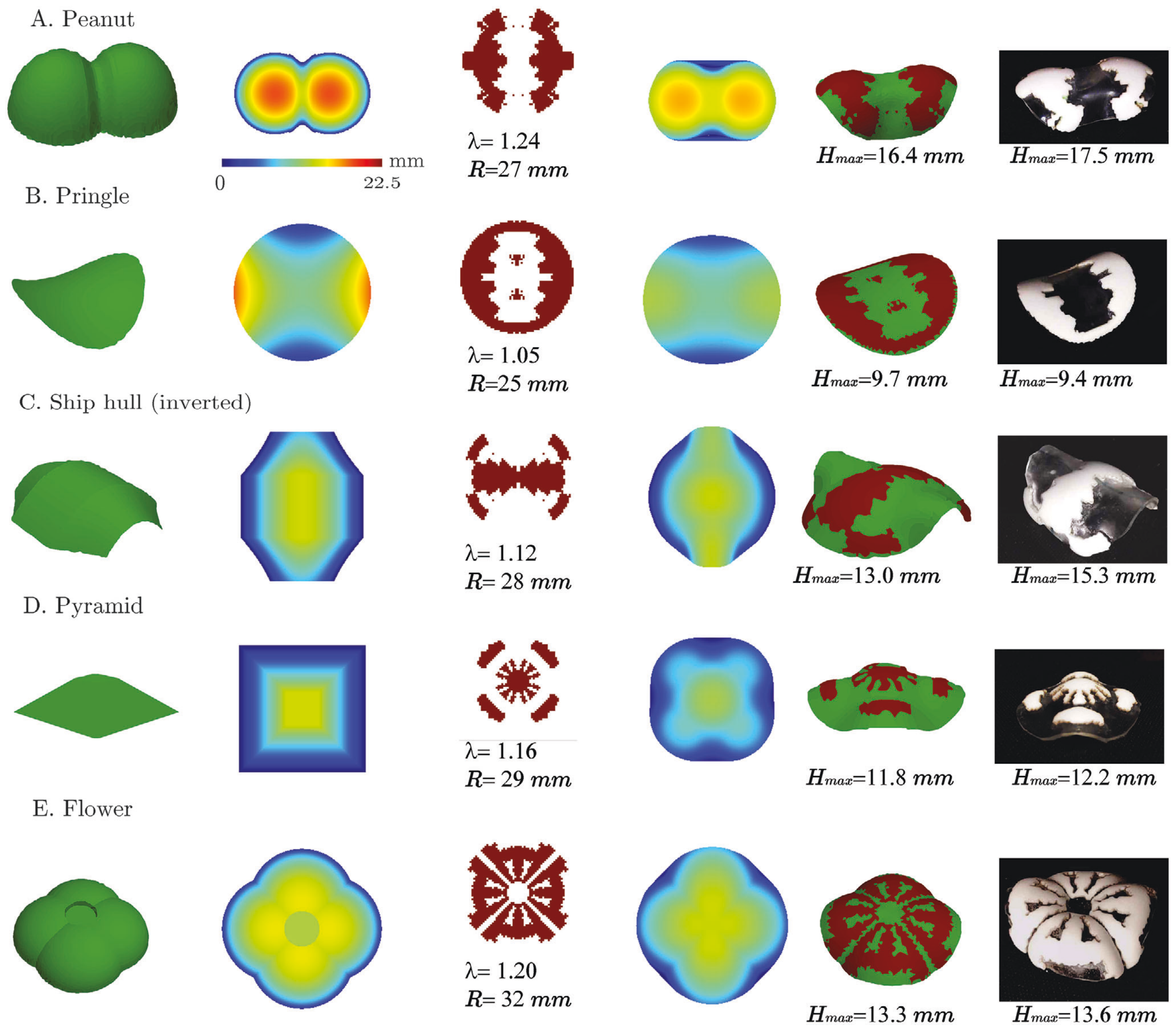

Figure 5. Inverse design framework: manufacturing programmable soft 3D structures. We illustrate the end to end design and manufacturing process. Target 3D shapes: the first column shows five different 3D shapes (a peanut, pringle, ship hull, pyramid, flower) input to the optimization algorithm. Height-coded 2D image representations: the second column shows distribution of height for the target 3D shape. Optimal design parameters: the third column presents the optimized kirigami patterns, prestretch, and radius selected after 100 iterations. Height-coded 2D image representations of the optimal predicted shapes: the fourth column presents the height distribution of predicted 3D topology obtained from finite element simulation using the optimal design parameters. The SSIM are approximately in 0.9. The predicted 3D shapes: the fifth column shows the predicted 3D shape in simulation. The maximum heights for the 3D images are shown in the bottom. Experimentally realized morphing 3D soft structures with desired shapes: the sixth column shows the experimental result of the 3D topology given the optimal parameters and following the manufacturing setup illustrated in Figure 3. [Correction added on February 5, 2024, after first online publication: figure 5 has been replaced in this version.]

maximum height of the free buckling shape, and R and t represent the radius and thickness of the planar structure, respectively (see **Figure 6**). We derive an analytical relationship by balancing the stretching-induced energy (pre-buckling) in the bottom layer and the bending-related energy dominated by the kirigami layer. We find that for a pyramid like 3D shape, the maximum normalized height H/R scales with $\frac{R}{t}\sqrt{\frac{E_s}{E_k}\frac{\epsilon}{1+\epsilon}}$ (see *Supporting Information Text*), where E_s and E_k are the Young's moduli of the substrate and the kirigami, respectively. Such a relationship can directly extend the design of soft composite structures from one maximum height to different heights by changing the original radius of the composite structures and prestretch.

As an example, we choose the optimized kirigami pattern that leads to a pyramid shape, and investigate how the normalized height is scaled with the variation of normalized radius and prestretch. Figure 6A shows the maximum normalized height H/R as a function of normalized radius R/t and prestretch. The star symbol in Figure 6A denotes the optimal combination of

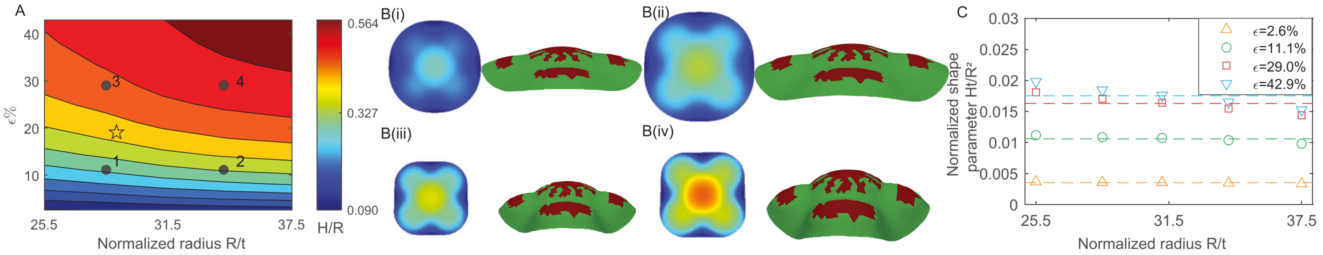

Figure 6. Scaling law and kirigami invariance: the same kirigami can be used to design target shapes with varying size parameters H/R by selecting prestretch and radius of the composite structure A) Distribution of H/R with the variation of size ratio R/t and the amount of applied prestretch ϵ. The star symbol denotes the optimal size and prestretch combination that gives the target pyramid shape. The black dots denote the regions where the size and prestretch is perturbed around the optimal point. B) Typical free buckling shapes that correspond to the black dots in (A) Both the height-coded 2D image representation and the corresponding 3D structure are presented. C) A normalized shape parameter Ht/R^2 as a function of normalized radius R/t at different amount of prestretch. The line horizontal dashed lines indicates the scaling prediction: H/R scales linearly with R/t.

prestretch and radius that leads to the target pyramid shape over 100 iterations. The black dots are the selected examples where the radius and prestretch are perturbed around the optimal values. If we want to design taller pyramids, we can slightly increase the normalized radius from Figure 6*B*(i) to (ii). When we slightly increase the prestretch around the optimal point from Figure 6*B*(i) to (iii), the height of the 3D shape also increases, but the radius of the deformed geometry decreases. Similar phenomena can be observed by varying from Figure 6*B*(ii) to (iv). The increase of H/R is proportional to the increase of the normalized radius R/t in Figure 6*C*. This agrees with the scaling analysis of elastic energies. When the prestretch is larger, the stretching energy in the deformed (i.e., post-buckling) configuration becomes larger, which causes H/R to deviate from the linear relationship with R/t. As R/t decreases, the more important the post-buckling stretching energy becomes, but such stretching energy is not considered in the current analytical derivation, which is based on balancing only the pre-buckling stretching energy. This suggests that the coupling between stretching and bending are important in these conditions, which needs more complicated models beyond the scaling analysis to explain the coupling and hence the shape variation. Similar phenomena are also found for other target shapes, such as flower and peanut, and more detailed discussion can be found in *Supporting Information Text*.

5.2. Importance of Symmetry

In this section, we aim to demonstrate that an arbitrarily constructed large class of kirigami patterns may still be limited in forming target 3D shapes. The free buckling shape assumed by the symmetry-constrained shapes and unidirectional strips, which doesn't guarantee the reflectional or fourfold radial symmetry, are compared. **Figure** 7*A* shows that even though the unidirectional strips are able to predict the ship hull like shape with reasonable accuracy, it fails to predict the flower shape in Figure 7*B*. The optimized kirigami patterns and the corresponding 3D shapes after 100 iterations are also compared with the target shape in Figure 7. Even though the VAE models can generate new patterns, with mixed combination of multi-directional strips, few of the generated patterns are exactly radially symmetric. This causes the free buckling shape to bend more in a preferred direction. The desired reflectional symmetry of a ship hull like target shape is also not guaranteed using the combinations of unidirectional strips. The comparisons demonstrate the importance of constraining the design space with appropriate symmetric property at the very beginning of the design process.

5.3. The Advantage of Proposed VAE and Bayesian Optimization Combined Approach Over Evolutionary Algorithms

We also compare the optimization results from the proposed framework with that using genetic algorithm (GA), which is a standard evolutionary algorithm (see *Supporting Information Text*). The purpose of the comparison is to compare the proposed machine learning-aided algorithm against traditional evolutionary search. In the evolutionary search, the inputs are not the latent variables. Instead, we have overall 16 input variables from the geometric, and material parameters. We set the variables to be 13 binary integers representing the presence of kirigami materials in the 13 divided regions in Figure S1 *A*(ii), *B*(ii), and *C*(ii) (Supporting Information). Another discrete integer is used to indicate the amount of rotation applied to the kirigami patterns, and two other continuous variables are introduced to represent the radius of the structure, and the amount of prestretch to be applied. The population size in the standard algorithm is chosen as ten, and the maximum number of iterations is set as 20. This means that we need to perform 200 numerical simulations per design; recall that this is twice the number of forward simulations used in our design framework, thus giving the GA approach a computational advantage.

Figure 7 compares the result of applying the genetic algorithm to the unidirectional or symmetric shapes. The comparison suggests that the proposed VAE and Bayesian Optimization combined approach can search the optimal combinations of kirigami and prestretch faster, and can achieve 3D deformed shapes closer to target shapes, compared to the evolutionary search. Without the VAE-aided reduced dimensional and continuous kirigami search space, the standard evolutionary optimization is limited to searching only the discrete design space. The comparison between the third and the fifth column of Figure 7*A, B* demonstrates that the incapability of generating new kirigami patterns beyond the input dataset restricts the conventional optimization

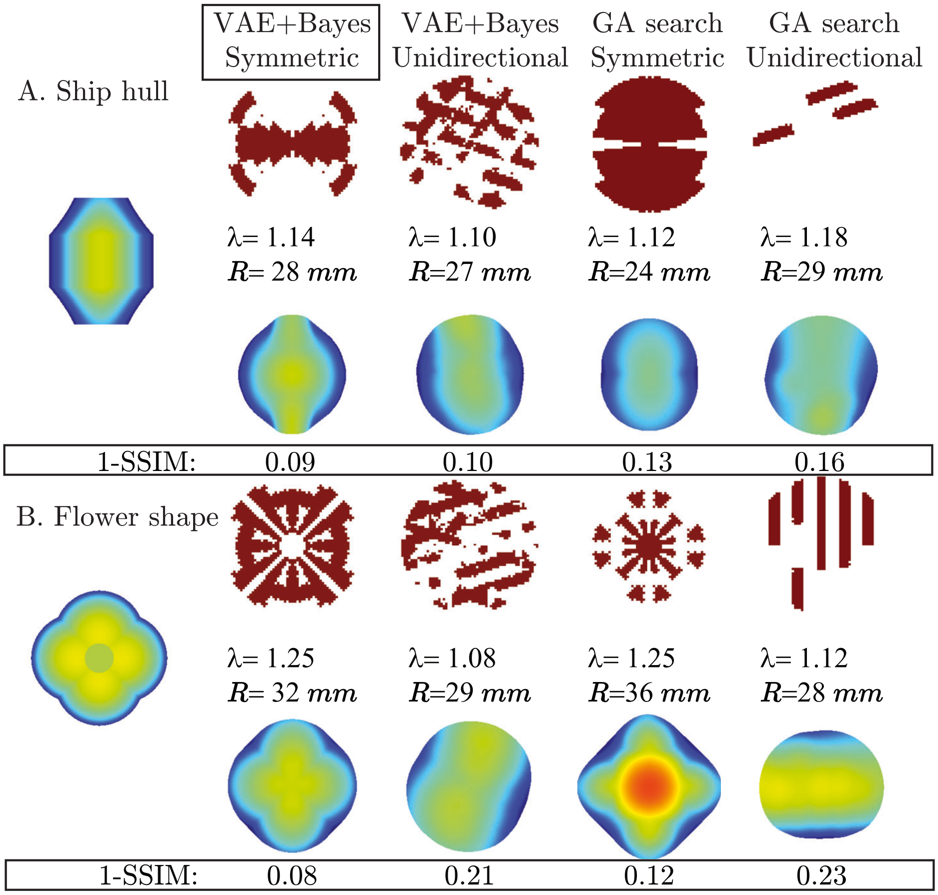

Figure 7. Comparison of the optimal kirigami patterns and height distribution of assumed 3D shape using different optimization methods. Target shapes: The first column shows the distribution of height for the target shapes, A) Ship hull B) Flower shape. The optimizations are conducted using four approaches. VAE+Bayesian optimization with symmetric patterns: the second column presents the optimal solution found in 100 iterations using VAE+Bayesian optimization with symmetric patterns. VAE+Bayesian optimization with unidirectional strips: the third column shows the optimal solution in 100 iterations using VAE+Bayesian optimization with unidirectional strips. Genetic algorithm with symmetric patterns: the fourth column shows the optimal solution in 200 iterations using genetic algorithm with symmetric patterns. Genetic algorithm with unidirectional strips: the fifth column shows the optimal solution in 200 iterations using genetic algorithm with unidirectional strips.

approaches from interpolating between the candidate kirigami patterns to achieve desired free buckling shapes.

5.4. Extension to General Target Shapes and Limitations of the Approach

There are a few limitations to the approach we employed. First, we are restricted to a circular substrate and uniform prestretch in the substrate. This limits the types of target shapes to those without sharp changes in local curvature. Second, so far, we have restricted ourselves to shapes that exhibit certain types of symmetry. To address this limitation, creating more generic patterns of the kirigami cuts is necessary. However, when dealing with target shapes featuring arbitrary symmetry and orientations, direct assessment of similarity becomes challenging. The predicted and target shapes have distinct centers of mass and orientations, requiring an extension of the metric to be orientation and translation invariant – a potential avenue for future research.

In an initial attempt to model more general shapes in **Figure** 8, our focus shifts to creating 3D shapes with only one axis of symmetry. To create kirigami patterns of one axis of symmetry, we use the six latent features to reconstruct the 2D kirigami pattern in half of the plane with reflectional symmetry, and use another six latent features to reconstruct the 2D kirigami pattern in the other half of the plane with reflectional symmetry. Consequently, the total number of features optimized amounts to 14, which includes the 12 latent features describing the kirigami patterns, a parameter for the radius of the substrate, and a parameter for the uniform prestretch.

To compare the similarity of 3D shapes, we align the center of mass of the target and predicted shapes before using the SSIM metric to measure their similarity. As an illustrative example, we applied this approach to create an asymmetric peanut shape in Figure 8*A* and a butterfly shape with only one symmetric axis in Figure 8*B*. The results suggest that within 200 iterations, the active learning approach effectively determines optimal kirigami patterns, radial prestretch, and structure size, achieving targeted 3D shapes with an SSIM of 0.9.

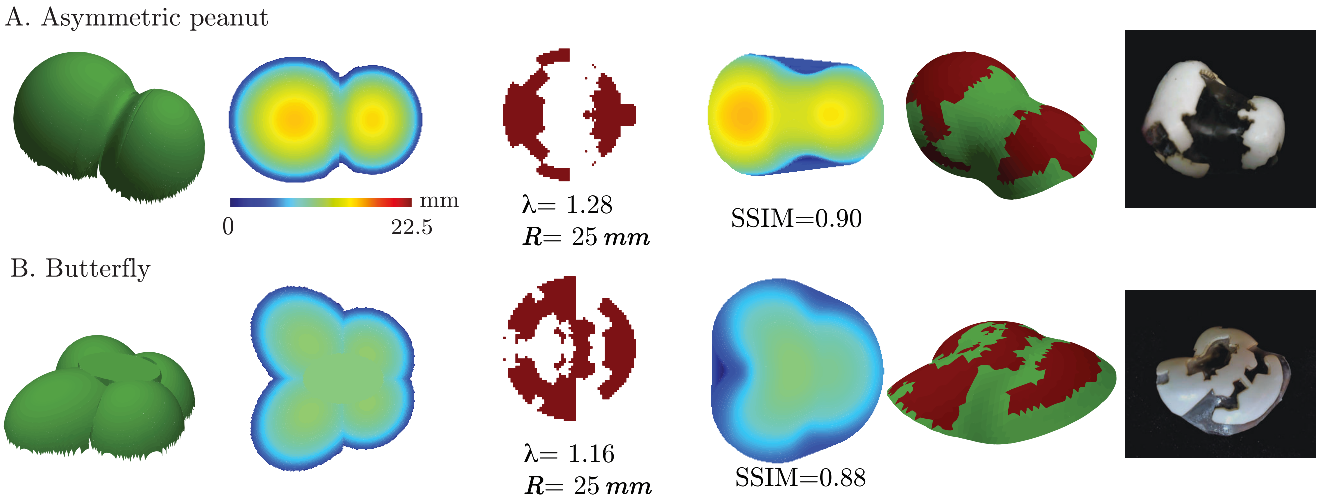

Figure 8. Inverse design framework with asymmetric soft 3D structures. Target 3D shapes: the first column shows two different 3D shapes (A) an asymmetric peanut and (B) a butterfly) as input to the optimization algorithm. These are asymmetric about an axis. Height-coded 2D image representations: the second column shows distribution of height for the target 3D shape. Optimal design parameters: the third column presents the optimized kirigami patterns, prestretch, and radius selected after 200 iterations. Height-coded 2D image representations of the optimal predicted shapes: the fourth column presents the height distribution of predicted 3D topology obtained from finite element simulation using the optimal design parameters. The SSIMs are approximately 0.9. The predicted 3D shapes: the fifth column shows the predicted 3D shape in simulation. The maximum heights for the 3D images are shown in the bottom. Experimentally realized morphing 3D soft structures with desired shapes: the sixth column shows the experimental result of the 3D topology given the optimal parameters and following the manufacturing setup illustrated in Figure 3.

5.5. 3D Scanning and Pointwise Comparison

We obtained 3D scans of the experimental structures from Figures 5 and 8 using a 0.1 mm resolution 3D scanner. The scanner gave us a point cloud (Cartesian coordinates of a large number of points on the surface of the structure), enabling a route to quantitative comparison with our computational framework. **Figure 9***A* shows a qualitative comparison between the experimental 3D scans (gray surface) with the predicted shape outputs (green point clouds) for seven different target shapes. For quantitative comparison, we introduce a relative error parameter, δ, that compares the z-coordinate of each point (representing the height of the point) in the 3D scan data with its numerical prediction. This parameter can be expressed as

$$\delta = \frac{1}{\max\left(\left|z^i_{\text{scan}}\right|\right)} \sum_{i=1}^{N_p} \frac{\left|z^i_{\text{pred}} - z^i_{\text{scan}}\right|}{N_p} \tag{1}$$

where N_p is the number of points in the point cloud, z^i_{scan} is the z-coordinate of the i-th point in the 3D scan data, and z^i_{pred} is the z-coordinate of the same point in the numerical predicted shape. The symbol $||$ indicates absolute value, and $\max(|z^i_{\text{scan}}|)$ is the maximum of the absolute values of the z-coordinates in the 3D scan data. Figure 9B shows a plot of this error metric across various shapes. The error is usually $\lesssim 10\%$ and the maximum deviation, that occurs for the ship, remains within 20%. We find this agreement to be excellent since the computational framework simulates the material using a hyperelastic model (Mooney-Rivlin) and ignores any viscous characteristics. In practice, there is a small amount of time dependent viscous deformation that was ignored. The Mooney-Rivlin model is phenomenological in nature and cannot capture the material with complete accuracy.

6. Concluding Remarks

We numerically and experimentally explored the capability of deforming a planar composite structure to target 3D shape via kirigami cutting and strain-mismatch. The design space is very high dimensional to be optimized directly. We formulated a VAE and active learning combined approach to tackle the design challenges. A VAE is used to represent originally high-dimensional design variables to a much lower dimensional continuous search space. The Bayesian optimization is then conducted to quickly obtain multiple optimal design solutions that achieve similar target free buckling shapes, ranging from shapes inspired by a peanut to a pyramid. We found that the nonlinear interplay between the strain mismatch, size of the composite structure, and the kirigami patterns strongly affect the free buckling shapes. We also studied the effect of imposing symmetry constraints on the machine learning-aided design results. The comparison of the results with and without symmetry constraints demonstrates that the symmetry constraints at the beginning of the machine learning process are important in better approximating the target shapes. A scaling law is used to guide scaling of the target shapes from one size to another, without having to search for the optimal design parameters. We also discussed the advantage of the proposed framework over traditional approaches, such as genetic algorithm. The proposed framework accelerates the design of a series of shape morphing, fully soft composite structures from weeks and months of running millions of simulations to a few hours of strategically examining around 100 examples.

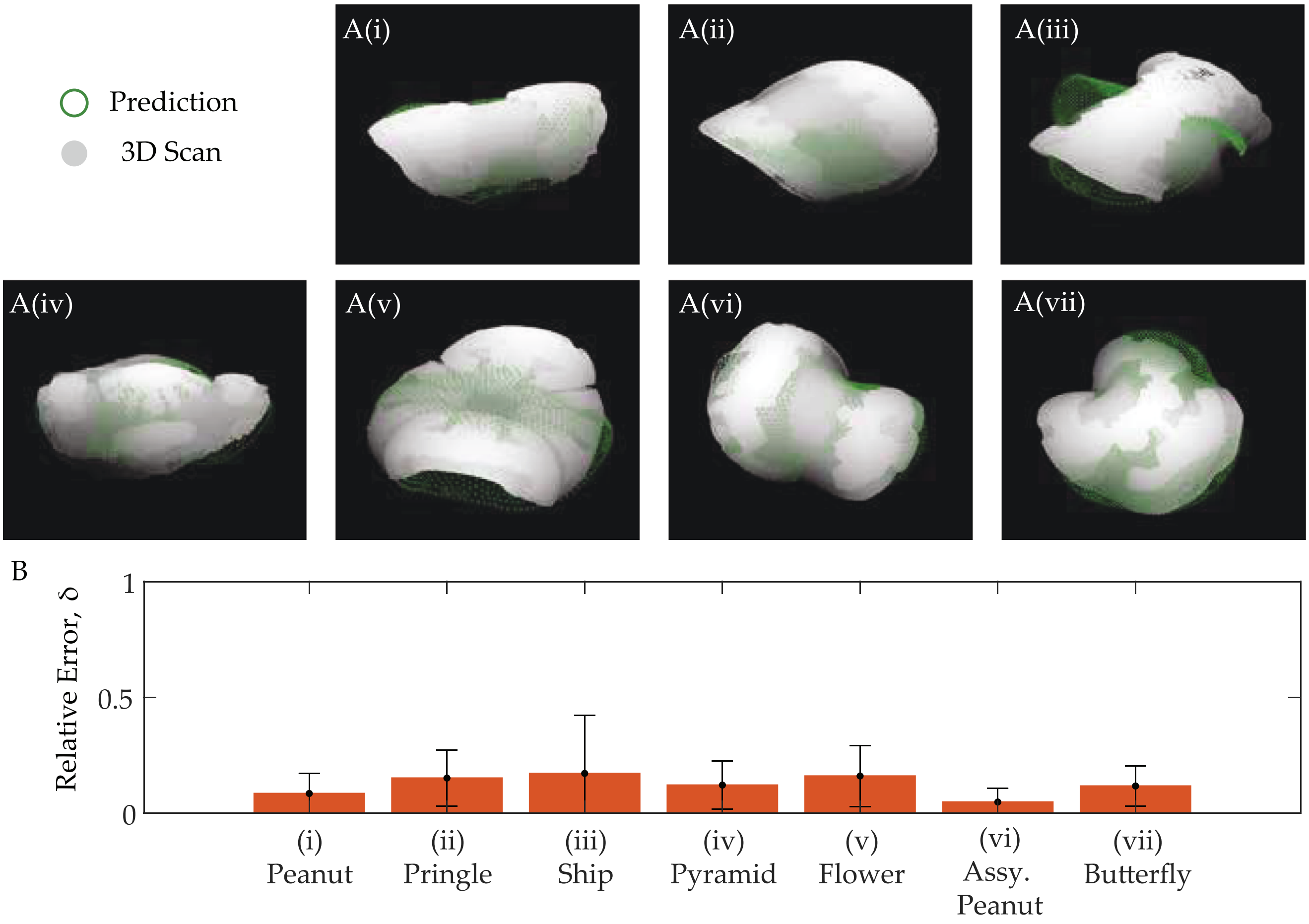

Figure 9. Comparison between experiments and numerical results. A) Qualitative comparison between the experimental 3D scans (gray surface) and the predicted shapes (green point cloud): (i) Peanut (ii) Pringle (iii) Ship (iv) Pyramid (v) Flower (vi) Asymmetric Peanut (vii) Butterfly. B) Quantitative comparison: The bar graph shows the relative error between experiments and numerics across various shapes considered in this paper. The error bars represent standard deviation of the error.

The inverse design method can provide a systematic way to solve a variety of form finding problems not limited to soft kirigami structures, but also to the manufacturing of gridshell[42,43] and compressive buckling-induced 3D architectures using micro ribbons[44] which can find applications in a range of areas including soft robotics, additive manufacturing, and architecture. In our future work, we plan to improve fabrication accuracy even further by potentially incorporating controls that can induce local deformations into our planar-only manufacturing platform.

7. Experimental Section

Bayesian Optimization: Bayesian optimization was a sample-efficient approach for solving a wide range of global optimization problems. See Ref. [33] for details; a short summary follows. This approach aims to solve an optimization, expressed as

$$\theta^* = \text{argmax}_\theta f\,(\theta) \tag{2}$$

where f is a black box model which is expensive to evaluate. The function was approximated by a Gaussian process model, rather than a neural network. Matern similarity kernel with homoscedastic noise was selected as the covariance of the likelihood function $\Phi(D|\theta)$. The noise in the function was also modeled as a Gaussian distribution $\Phi_{prior}(\theta)$, which had zero mean and variance chosen as 0.0001.

Given the available data D, the posterior distribution of the parameters $\Phi(\theta|D)$ is computed via the Bayes' theorem,

$$\Phi(\theta|D) \propto \Phi(D|\theta)\Phi_{prior}(\theta) \tag{3}$$

Based on the current posterior distribution, the acquisition function EI can be calculated as,

$$EI(\theta) = \mathbb{E}[u(\theta)] = \mathbb{E}[[f(\theta) - f(\theta_t^*)]^+] \tag{4}$$

where $\mathbb{E}$ is computing the expectation, θ_t^* is the best point observed so far. When $f(\theta) > f(\theta_t^*)$, $u(\theta) = f(\theta) - f(\theta_t^*)$. While when $f(\theta) \leq f(\theta_t^*)$, $f(\theta_t^*) = 0$. The next data to be sampled θ_{t+1} is selected such that the acquisition function was maximized, i.e., $\theta_{t+1} = argmax_\theta\ EI\,(\theta)$. Then, the Gaussian process and acquisition functions were updated. Such a process iterates several times until the optimal solution converges. Since the expected improvement function was increasing with both the mean prediction of the unknown black box model f and the uncertainty of the model.[33] Hence, by maximizing the Expected Improvement function, global optimums could be quickly searched rather than being stuck with specific local minimums.

The algorithm was implemented using the Scikit-Optimize package.

Supporting Information

Supporting Information is available from the Wiley Online Library or from the author.

Acknowledgements

The authors thank Shyan Shokrzadeh and Vishal Kackar for their assistance on experiments. The following research grants are gratefully acknowledged: NSF (CMMI-2053971) for L.M., M.M., V.R., and M.K.J.; and NSF (CAREER-2047663, CMMI-2101751) for M.K.J.

Conflict of Interest

The authors declare no conflict of interest.

Author Contributions

V.R. and M.K.J. designed research; L.M., and M.M. performed research; L.M. analyzed data; L.M., M.M., V.R., and M.K.J. wrote the paper.

Data Availability Statement

The data that support the findings of this study are available from the corresponding author upon reasonable request.

Keywords

active learning, form-finding, kirigami, mechanical instability, shell buckling

Received: September 4, 2023
Revised: December 8, 2023

[1] J. W. Boley, W. M. van Rees, C. Lissandrello, M. N. Horenstein, R. L. Truby, A. Kotikian, J. A. Lewis, L. Mahadevan, *Proc. Natl. Acad. Sci.* **2019**, *116*, 20856.
[2] Y. Tang, J. Yin, *Adv. Mater. Technol.* **2018**, *3*, 1800069.
[3] M. A. Dias, M. P. McCarron, D. Rayneau-Kirkhope, P. Z. Hanakata, D. K. Campbell, H. S. Park, D. P. Holmes, *Soft Matter* **2017**, *13*, 9087.
[4] L. Tomholt, O. Geletina, J. Alvarenga, A. V. Shneidman, J. C. Weaver, M. C. Fernandes, S. A. Mota, M. Bechthold, J. Aizenberg, *Energy and Build.* **2020**, *226*, 110377.
[5] J. Panetta, M. Konaković-Luković, F. Isvoranu, E. Bouleau, M. Pauly, *ACM Trans. Graph. (TOG)* **2019**, *38*, 1.
[6] S. Abdelmohsen, S. Adriaenssens, R. El-Dabaa, S. Gabriele, L. Olivieri, L. Teresi, *Comput.-Aided Des.* **2019**, *106*, 43.
[7] S. Xu, Z. Yan, K.-I. Jang, W. Huang, H. Fu, J. Kim, Z. Wei, M. Flavin, J. McCracken, R. Wang, A. Badea, Y. Liu, D. Xiao, G. Zhou, J. Lee, H. U. Chung, H. Cheng, W. Ren, A. Banks, X. Li, U. Paik, R. G. Nuzzo, Y. Huang, Y. Zhang, J. A. Rogers, *Science* **2015**, *347*, 154.
[8] J. Kim, J. A. Hanna, M. Byun, C. D. Santangelo, R. C. Hayward, *Science* **2012**, *335*, 1201.
[9] A. E. Forte, P. Z. Hanakata, L. Jin, E. Zari, A. Zareei, M. C. Fernandes, L. Sumner, J. Alvarez, K. Bertoldi, *Adv. Funct. Mater.* **2022**, *32*, 2111610.
[10] S. Felton, M. Tolley, E. Demaine, D. Rus, R. Wood, *Science* **2014**, *345*, 644.
[11] M. Pezzulla, G. P. Smith, P. Nardinocchi, D. P. Holmes, *Soft Matter* **2016**, *12*, 4435.
[12] C. Baek, A. O. Sageman-Furnas, M. K. Jawed, P. M. Reis, *Proc. Natl. Acad. Sci.* **2018**, *115*, 75.
[13] M. Liu, L. Domino, D. Vella, *Soft Matter* **2020**, *16*, 7739.
[14] Z. Fan, Y. Yang, F. Zhang, Z. Xu, H. Zhao, T. Wang, H. Song, Y. Huang, J. A. Rogers, Y. Zhang, *Adv. Mater.* **2020**, *32*, 1908424.
[15] W. M. Van Rees, E. Vouga, L. Mahadevan, *Proc. Natl. Acad. Sci.* **2017**, *114*, 11597.
[16] X. Dang, F. Feng, P. Plucinsky, R. D. James, H. Duan, J. Wang, *Int. J. Solids Struct.* **2022**, *234*, 111224.
[17] J. Wang, J. Suo, A. Chortos, *IEEE Robot. Autom. Lett.* **2021**, *7*, 549.
[18] R. Guseinov, E. Miguel, B. Bickel, *ACM Trans. Graph. (TOG)* **2017**, *36*, 1.
[19] R. Guseinov, C. McMahan, J. Pérez, C. Daraio, B. Bickel, *Nat. Commun.* **2020**, *11*, 237.
[20] G. P. Choi, L. H. Dudte, L. Mahadevan, *Nat. Mater.* **2019**, *18*, 999.
[21] M. Moshe, E. Esposito, S. Shankar, B. Bircan, I. Cohen, D. R. Nelson, M. J. Bowick, *Phys. Rev. Lett.* **2019**, *122*, 048001.
[22] Y. Zhang, Z. Yan, K. Nan, D. Xiao, Y. Liu, H. Luan, H. Fu, X. Wang, Q. Yang, J. Wang, W. Ren, H. Si, F. Liu, L. Yang, H. Li, J. Wang, X. Guo, H. Luo, L. Wang, Y. Huang, J. A. Rogers, *Proc. Natl. Acad. Sci.* **2015**, *112*, 11757.
[23] J. Tao, H. Khosravi, V. Deshpande, S. Li, *Adv. Sci.* **2023**, *10*, 2204733.
[24] D. P. Holmes, *Curr. Opin. Colloid Interface Sci.* **2019**, *40*, 118.
[25] L. Stein-Montalvo, P. Costa, M. Pezzulla, D. P. Holmes, *Soft Matter* **2019**, *15*, 1215.
[26] J. Zavodnik, Y. Wang, W. Yan, M. Brojan, M. K. Jawed, *arXiv preprint arXiv:2301.06597* **2023**, *1*, 1.
[27] P. Z. Hanakata, E. D. Cubuk, D. K. Campbell, H. S. Park, *Phys. Rev. Res.* **2020**, *2*, 042006.
[28] R. Danhaive, C. T. Mueller, *Autom. Constr.* **2021**, *127*, 103664.
[29] Y. Mao, Q. He, X. Zhao, *Sci. Adv.* **2020**, *6*, eaaz4169.
[30] Z. Liu, D. Zhu, S. P. Rodrigues, K.-T. Lee, W. Cai, *Nano Lett.* **2018**, *18*, 6570.
[31] P. Z. Hanakata, E. D. Cubuk, D. K. Campbell, H. S. Park, *Phys. Rev. Lett.* **2018**, *121*, 255304.
[32] R. Xue, R. Li, Z. Du, W. Zhang, Y. Zhu, Z. Sun, X. Guo, *Extreme Mech. Lett.* **2017**, *15*, 139.
[33] P. I. Frazier, *arXiv preprint arXiv:1807.02811* **2018**, https://doi.org/10.48550/arXiv.1807.02811.
[34] J. D. Paulsen, E. Hohlfeld, H. King, J. Huang, Z. Qiu, T. P. Russell, N. Menon, D. Vella, B. Davidovitch, *Proc. Natl. Acad. Sci.* **2016**, *113*, 1144.
[35] T. C. Shyu, P. F. Damasceno, P. M. Dodd, A. Lamoureux, L. Xu, M. Shlian, M. Shtein, S. C. Glotzer, N. A. Kotov, *Nat. Mater.* **2015**, *14*, 785.
[36] A. Rafsanjani, K. Bertoldi, *Phys. Rev. Lett.* **2017**, *118*, 084301.
[37] B. Burger, P. M. Maffettone, V. V. Gusev, C. M. Aitchison, Y. Bai, X. Wang, X. Li, B. M. Alston, B. Li, R. Clowes, N. Rankin, B. Harris, R. S. Sprick, A. I. Cooper, *Nature* **2020**, *583*, 237.
[38] E. Ahmed, A. Saint, A. E. R. Shabayek, K. Cherenkova, R. Das, G. Gusev, D. Aouada, B. Ottersten, *arXiv preprint arXiv:1808.01462* **2018**, https://doi.org/10.48550/arXiv.1808.01462.
[39] H. Zhao, O. Gallo, I. Frosio, J. Kautz, *IEEE Trans. comput. imaging* **2016**, *3*, 47.

[40] M. Smith, *ABAQUS/Standard User's Manual, Version 6.9*, Dassault Systèmes Simulia Corp, Providence, RI **2009**.

[41] F. Pedregosa, G. Varoquaux, A. Gramfort, V. Michel, B. Thirion, O. Grisel, M. Blondel, P. Prettenhofer, R. Weiss, V. Dubourg, J. Vanderplas, A. Passos, D. Cournapeau, M. Brucher, M. Perrot, É. Duchesnay, *J. Mach. Learn. res.* **2011**, *12*, 2825.

[42] L. Qin, W. Huang, Y. Du, L. Zheng, M. K. Jawed, *Structural and Multidisciplinary Optimization* **2020**, *62*, 2691.

[43] F. Isvoranu, J. Panetta, T. Chen, E. Bouleau, M. Pauly, in *Proceedings of IASS Annual Symposia*, volume *2019*. International Association for Shell and Spatial Structures (IASS), Barcelona, Spain **2019**, pp. 1–8, https://infoscience.epfl.ch/record/296477 .

[44] H. Luan, Q. Zhang, T.-L. Liu, X. Wang, S. Zhao, H. Wang, S. Yao, Y. Xue, J. W. Kwak, W. Bai, Y. Xu, M. Han, K. Li, Z. Li, X. Ni, J. Ye, D. Choi, Q. Yang, J.-H. Kim, S. Li, S. Chen, C. Wu, D. Lu, J.-K. Chang, Z. Xie, Y. Huang, J. A. Rogers, *Sci. Adv.* **2021**, *7*, eabj3686.